



Article

Estimation of All-Day Aerosol Optical Depth in the Beijing–Tianjin–Hebei Region Using Ground Air Quality Data

Wenhao Zhang ^{1,2} , Sijia Liu ^{1,2}, Xiaoyang Chen ^{1,2}, Xiaofei Mi ^{3,*} , Xingfa Gu ^{1,3} and Tao Yu ^{1,3}

¹ School of Remote Sensing and Information Engineering, North China Institute of Aerospace Engineering, Langfang 065000, China; zhangwh@radi.ac.cn (W.Z.); liusijia1007@stumail.ncaie.edu.cn (S.L.); chenxiaoyang0926@stumail.ncaie.edu.cn (X.C.); guxf@aircas.ac.cn (X.G.); yutao@radi.ac.cn (T.Y.)

² Hebei Collaborative Innovation Center for Aerospace Remote Sensing Information Processing and Application, Langfang 065000, China

³ Aerospace Information Research Institute, Chinese Academy of Sciences, Beijing 100094, China

* Correspondence: mixf@aircas.ac.cn

Abstract: Atmospheric aerosols affect climate change, air quality, and human health. The aerosol optical depth (AOD) is a widely utilized parameter for estimating the concentration of atmospheric aerosols. Consequently, continuous AOD monitoring is crucial for environmental studies. However, a method to continuously monitor the AOD throughout the day or night remains a challenge. This study introduces a method for estimating the All-Day AOD using ground air quality and meteorological data. This method allows for the hourly estimation of the AOD throughout the day in the Beijing–Tianjin–Hebei (BTH) region and addresses the lack of high temporal resolution monitoring of the AOD during the nighttime. The results of the proposed All-Day AOD estimation method were validated against AOD measurements from Advanced Himawari Imager (AHI) and Aerosol Robotic Network (AERONET). The R^2 between the estimated AOD and AHI was 0.855, with a root mean square error of 0.134. Two AERONET sites in BTH were selected for analysis. The results indicated that the absolute error between the estimated AOD and AERONET was within acceptable limits. The estimated AOD showed spatial and temporal trends comparable to those of AERONET and AHI. In addition, the hourly mean AOD was analyzed for each city in BTH. The hourly mean AOD in each city exhibits a smooth change at night. In conclusion, the proposed AOD estimation method offers valuable data for investigating the impact of aerosol radiative forcing and assessing its influence on climate change.

Keywords: All-Day; Aerosol Optical Depth (AOD); XGBoost; Beijing–Tianjin–Hebei region



Citation: Zhang, W.; Liu, S.; Chen, X.; Mi, X.; Gu, X.; Yu, T. Estimation of All-Day Aerosol Optical Depth in the Beijing–Tianjin–Hebei Region Using Ground Air Quality Data. *Remote Sens.* **2024**, *16*, 1410. <https://doi.org/10.3390/rs16081410>

Academic Editors: Costas Varotsos and Alexander Kokhanovsky

Received: 4 February 2024

Revised: 5 April 2024

Accepted: 10 April 2024

Published: 16 April 2024



Copyright: © 2024 by the authors. Licensee MDPI, Basel, Switzerland. This article is an open access article distributed under the terms and conditions of the Creative Commons Attribution (CC BY) license (<https://creativecommons.org/licenses/by/4.0/>).

1. Introduction

Atmospheric aerosols are multiphase systems comprising solid or liquid particles suspended in gaseous media [1]. These aerosols significantly influence the Earth's radiation balance, air quality, and human health [2]. The impact on the Earth's radiation balance can be direct through the scattering and absorption of solar radiation and indirect through changes in cloud properties [3–5]. Aerosols play a pivotal role in determining air quality. When the atmosphere contains high concentrations of aerosol particles, the particles will scatter and absorb light. Consequently, the presence of haze or cloudy air can significantly reduce visibility and affect daily activities [6,7]. Concurrently, air pollution can also influence the structural integrity and durability of materials [8,9]. Certain aerosols pose health risks [10]. For example, fine particles with a diameter smaller than 2.5 μm can penetrate the human respiratory system and accumulate in the lungs, causing respiratory and other health issues [11,12].

Atmospheric aerosols are derived from various sources and exhibit spatial and temporal variations [13,14]. Therefore, the real-time monitoring of atmospheric aerosols is

crucial for evaluating their impact. Ground-based and satellite-based methods are currently the primary methods used for aerosol monitoring [15]. Ground-based monitoring provides highly accurate aerosol data. The Aerosol Robotic Network (AERONET) uses a day-sky-moon photometer to continuously monitor atmospheric aerosols during the day and night [16]. Satellite monitoring is commonly used for the large-scale monitoring of aerosols. Aerosol retrieval has been conducted using various sensors, including the dark pixel method [17,18], deep blue algorithm [19], and other techniques adapted to specific surface features and aerosol types. These approaches have produced aerosol datasets with improved accuracy and spatial-temporal resolutions, such as Moderate Resolution Imaging Spectroradiometer (MODIS) and Advanced Himawari Imager (AHI) aerosol optical depth (AOD). Recent advancements in sensor technology have expanded the capabilities of satellite aerosol monitoring from low to high resolution, from day to night. High-resolution satellite sensors are frequently employed to facilitate precise aerosol monitoring following cross-calibration with reference sensors [20,21]. As the sensitivity of sensors escalates, the utilization of nighttime band information becomes viable for aerosol retrieval research. Zhang et al. [22] showed that it is feasible to retrieve the AOD at night by detecting the attenuation level in the visible/near-infrared band during nighttime hours. Johnson et al. [23] established a correlation between the AOD and upward radiation emitted from urban light sources by analyzing upward radiation within different light source areas. Jiang et al. [24] studied the potential of using NPP/VIIRS DNB low-light channels to monitor the AOD over North China and examined the distribution of urban lights and aerosols at night. Li et al. [25] acknowledged the challenges associated with the uncertainty of urban lights and proposed a method to enhance the precision of AOD retrieval. This method utilizes combined measurements of satellite low-light channel data and ground-based integrating spheres.

Although progress has been made in the retrieval of the AOD during the day and at night, there is still a gap in aerosol products that can cover a wide area of the globe and ensure continuous observation throughout the day. AERONET provides high-precision AOD data [26]. However, the limited number and uneven distribution of AERONET sites render large-scale ground-based aerosol monitoring impractical. Polar-orbiting satellites cannot continuously monitor aerosols because of their limited field of view and revisit times [27,28]. For example, MODIS collects only aerosol properties twice a day [29], whereas VIIRS transmits data only at 1:30 am local nighttime overpasses [30]. In contrast, geostationary satellites have a higher temporal resolution [31]. However, because of variations in the solar zenith angle, AOD retrieval cannot always be performed. For instance, the AHI AOD may fail to retrieve solar zenith angles exceeding 70° [32]. Moreover, ground-based and satellite monitoring often experience data gaps during meteorological conditions such as cloud cover, precipitation, and snowfall [33]. Nighttime aerosol monitoring faces several challenges. The CE318 developed by the French company Cimel Electronique instrument used by AERONET has many problems during nighttime measurements. The AOD measured using the CE318 instrument does not have quality assurance [34,35]. In addition, the CE318 instrument can only be used for nighttime observations when lunar illumination exceeds 50%. Therefore, even under optimal observation conditions, the instrument can cover only 50% of the monthly nighttime hours [16]. The accuracy of the nighttime AOD retrieval algorithm may be affected by the use of satellite low-light data because of the uncertainty caused by the radiant brightness of city lights and their obvious time-varying characteristics [25]. The lack of reliable nighttime aerosol data impedes the accurate assessment of nighttime aerosol climatic effects and their subsequent environmental implications. In some instances, researchers have chosen to utilize daytime AOD approximations instead of nighttime AOD. This can lead to data errors that directly affect the reliability and applicability of the study. Therefore, it is necessary to develop an All-Day aerosol-monitoring method.

Atmospheric aerosol particles are primarily classified into two categories: primary aerosols, which are emitted directly into the atmosphere from emission sources; and sec-

ondary aerosols, which are generated by the atmospheric chemical reactions of primary aerosols with gaseous components. As most atmospheric aerosols originate from particulate matter or its chemical reactions with gaseous pollutants, the concentrations of major atmospheric pollutants affect aerosol concentrations [36,37]. However, the correlation between the AOD and ground air quality data is not a straightforward linear relationship. The AOD is the integral of the radiative extinction caused by aerosols from the surface to the top of the atmosphere at a given wavelength. Ground air quality data are concentrations of air pollutants measured under dry conditions. This relationship between the AOD and ground air quality data is influenced by many factors, including meteorological conditions [38,39]. Many studies have delved into the correlation between PM and the AOD, as well as its potential implications [40,41]. For instance, Seo et al. [42] elucidated the correlation between the PM₁₀ concentration and AOD by incorporating several parameters into an empirical model. These parameters include the boundary layer height, relative humidity, and the effective radius of the aerosol particle size distribution. Zheng et al. [43] conducted a comprehensive analysis of the influence of various factors on aerosol distribution in the Beijing region, utilizing ground-based and satellite observations spanning 2011 to 2015. These factors included the type of aerosol, relative humidity, planetary boundary layer height, wind speed and direction, as well as the vertical structure of aerosols. The authors adjusted for the vertical extension and hygroscopic growth effects of aerosols by incorporating the boundary layer height and relative humidity. However, the processes of aerosol formation, diffusion, migration, and transformation are complex and variable. Consequently, the establishment of a relationship between the AOD and ground air quality data requires the consideration of multifactorial influences.

Ground air quality sites cover the primary study area and provide continuous hourly data on critical atmospheric pollutants. Therefore, this study aimed to develop an All-Day AOD estimation model (All-Day AODES) using ground air quality data and meteorological data. This study presents a valuable tool for estimating the AOD and provides data support for research on aerosol radiative forcing effects, climate change, and related areas. By analyzing and discussing the spatial and temporal distributions and the diurnal variations in the estimated AOD, this study aims to enhance our understanding of aerosol dynamics.

2. Materials and Methods

2.1. Datasets

2.1.1. Ground Air Quality Data

The Beijing–Tianjin–Hebei (BTH) region is located on the North China Plain. It spans from 113.3–119.5°E to 36–42.4°N. This region is a pivotal economic and cultural nexus within China, ranking among the country's most advanced areas. Nevertheless, it has persistently grappled with severe atmospheric environmental challenges due to the confluence of natural elements, namely its geographical positioning and climatic conditions, and anthropogenic influences, such as industrialization and transportation. Figure 1 shows the geographical position and elevation of BTH.

The China National Environmental Monitoring Center plays a vital role in assessing air pollution levels, and monitoring and issuing air pollution event alerts. It provides hourly data from ground air quality sites including PM_{2.5}, PM₁₀, SO₂, NO₂, O₃, and CO. Figure 1 shows the spatial distribution of 135 ground air quality sites across BTH. Data with missing or negative values were excluded to ensure the credibility of the experiment. The experimental data time range is 00:00 on 1 January 2020 to 23:00 on 31 December 2020. In 2020, 648,850 valid data points were collected, accounting for 90% of the total dataset. A large amount of data indicate sufficient data for the analysis.

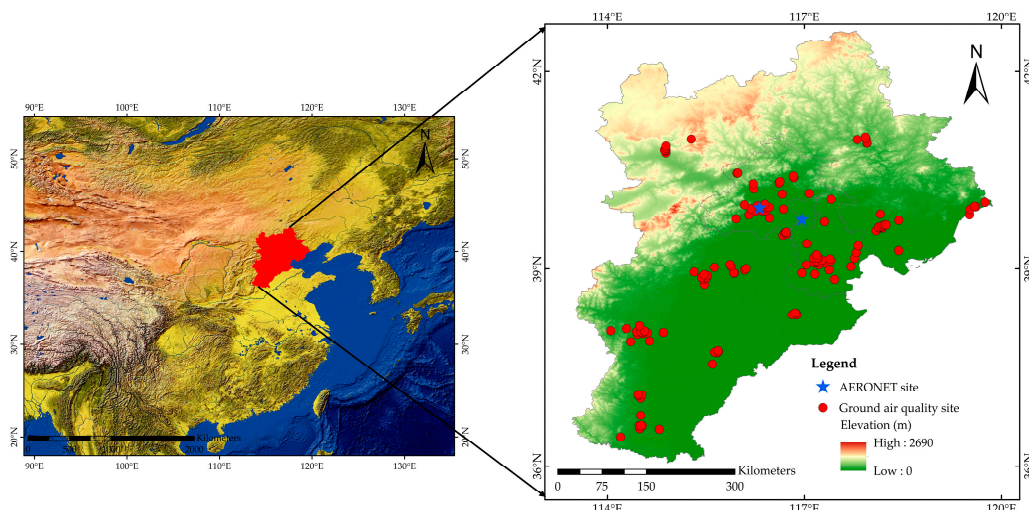


Figure 1. BTH location, elevation information, and distribution of AERONET sites and ground air quality sites in the region. Blue stars are AERONET sites and red dots are ground air quality sites.

2.1.2. Meteorological Data

ERA5, developed by the European Centre for Medium-Range Weather Forecasts, represents the most recent generation of reanalysis data [44]. This ERA5 includes hourly single- and pressure-level data and has been consistently published since 1940. It provides meteorological data at a spatial resolution of 0.25° . In this study, we specifically employed hourly data for relative humidity (RH) at 1000 hPa, boundary layer height (BLH), surface pressure (SP), 2 m temperature (T2M), 10 m u-component (U10), and 10 m v-component (V10) of wind for 2020.

2.1.3. AHI AOD

The AHI is an optical payload aboard the Himawari-8 satellite. The AHI AOD dataset incorporates L3-level retrieval results at a wavelength of 500 nm. This dataset has a spatial resolution of 0.05° and a temporal resolution of 1 h. This study employed the L3-level AOD dataset from satellite observations, specifically selecting AOT_Merged and its associated aerosol labeling data, QA_flag_merged. These datasets were obtained through meticulous cloud screening and the subsequent spatial-temporal interpolation of the L2-level AOD.

The AOD confidence In QA_flag_merged was divided into four levels: excellent, good, marginal, and no confidence [31]. To ensure the quality of the AOD in this study, only excellent and good labels were selected.

2.1.4. AERONET AOD

AERONET has more than 500 sites covering major regions of the world. AERONET uses a CIMEL CE318 multiband photometer to perform long-term AOD observations. The high accuracy of AERONET AOD is often used as a reference value for validating remote sensing AOD. The AERONET Version 3 AOD was computed for three data quality levels: 1.0 (unscreened), 1.5 (cloud-screened and quality-controlled), and 2.0 (quality-assured) [45]. The accuracy of the daytime estimated results was verified using Level 1.5 AOD at 500 nm. Table 1 shows the information of the AERONET sites used. Figure 1 illustrates the distribution of AERONET sites in BTH.

Table 1. Latitude and longitude information of AERONET sites in BTH.

Site	Latitude/ $^\circ$ N	Longitude/ $^\circ$ E
XiangHe	39.754	116.962
Beijing-CAMS	39.933	116.317

2.2. Methods

Figure 2 shows a flowchart of the method used in this study to estimate the AOD in BTH. This process includes several steps: data collection and preprocessing, sample dataset construction, All-Day AODES development, model evaluation, and AOD estimation.

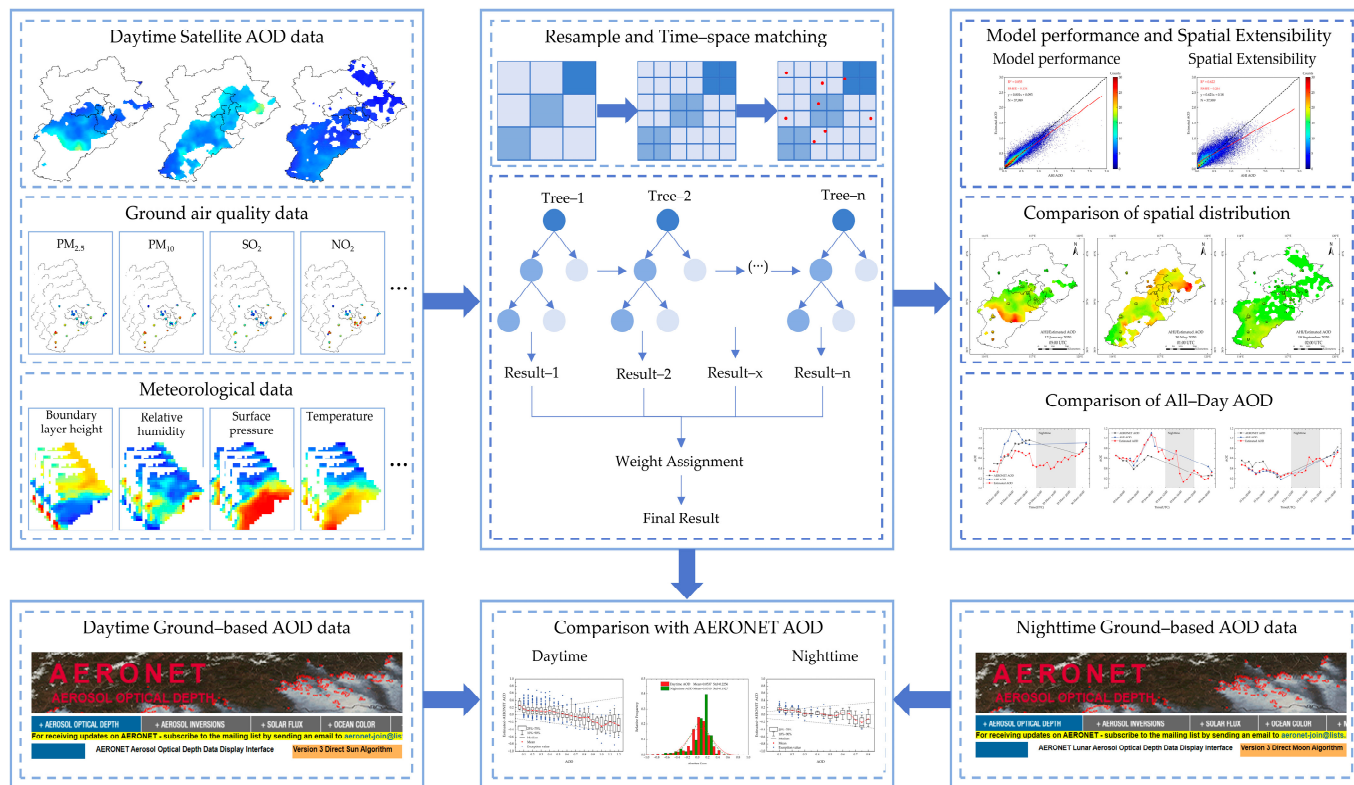


Figure 2. A flowchart of the overall structure of the study.

2.2.1. Data Preprocessing

This study used ground air quality, meteorological, and daytime satellite AOD data. Table 2 lists the integrated datasets used in this study. To ensure consistent data analysis, it is necessary to harmonize the spatial-temporal dimensions when integrating data from diverse sources. Meteorological data were interpolated using bilinear interpolation to achieve a uniform spatial resolution of 0.05°. Ground air quality data were converted from Beijing time (UTC + 8) to Coordinated Universal Time (UTC). To facilitate a comparison between the estimated, AHI, and AERONET AOD, the AHI and AERONET AOD at 500 nm were selected. During the process of merging the datasets, data with missing or negative values were excluded.

Table 2. Descriptive statistics of the dataset.

Category	Variable	Content	Units	Spatial Resolution	Temporal Resolution
Ground air quality data	PM _{2.5}	Particulate matter ≤ 2.5 μm 1 h average	μg/m ³	site	Hourly
	PM ₁₀	Particulate matter ≤ 10 μm 1 h average	μg/m ³	site	Hourly
	SO ₂	SO ₂ 1 h average	μg/m ³	site	Hourly
	NO ₂	NO ₂ 1 h average	μg/m ³	site	Hourly
	O ₃	O ₃ 1 h average	μg/m ³	site	Hourly

Table 2. Cont.

Category	Variable	Content	Units	Spatial Resolution	Temporal Resolution
Meteorological data	BLH	Boundary layer height	m	$0.25^\circ \times 0.25^\circ$	Hourly
	SP	Surface pressure	Pa	$0.25^\circ \times 0.25^\circ$	Hourly
	T2M	2 m temperature	K	$0.25^\circ \times 0.25^\circ$	Hourly
	U10	10 m u–component of wind	m/s	$0.25^\circ \times 0.25^\circ$	Hourly
	V10	10 m v–component of wind	m/s	$0.25^\circ \times 0.25^\circ$	Hourly
	RH	Relative humidity	%	$0.25^\circ \times 0.25^\circ$	Hourly
Satellite AOD data	AOD	Aerosol Optical Depth	–	$0.05^\circ \times 0.05^\circ$	Hourly

2.2.2. All-Day AODES

In this study, the All-Day AODES was constructed using ground air quality data and meteorological data. Meteorological data, such as BLH, SP, T2M, U10, V10, and RH, were taken into account. The RH, BLH, and T2M affected the vertical distribution of aerosol particles and absorption differences. The U10, V10, and SP affected the flow rate and direction of the atmosphere, which in turn affected the transport and diffusion processes of aerosols. The impacts of surface air pollutants were assessed through ground-based monitoring of $PM_{2.5}$, PM_{10} , SO_2 , NO_2 , and O_3 .

The processes of aerosol formation, diffusion, migration, and transformation are complex and variable. These processes exhibit significant nonlinear characteristics, which make it challenging to accurately estimate their concentrations using a simple linear model. Machine learning algorithms are not only straightforward to implement but also offer rapid computational capabilities. Furthermore, they exhibit a high tolerance for outliers and noise, making them particularly adept at addressing nonlinear problems. Therefore, the All-Day AODES proposed in this study is based on machine learning algorithms.

The All-Day AODES was based on XGBoost (1.6.2). Figure 3 shows the structure of the XGBoost model. The XGBoost algorithm iteratively adds trees and performs feature splitting to grow each tree. At each iteration, a new tree is added to capture the residuals of the previous prediction. Based on the sample characteristics, it was assigned to a specific leaf node in each tree, which corresponded to a score. Finally, the predicted value for the sample was obtained by summing the scores for each tree [46–48]. The relationships between the features and targets in the training set were trained and learned using the selected regression algorithms.

This study employed Bayesian optimization to determine the optimal hyperparameters of the model. Bayesian optimization involves updating the posterior distribution of the objective function through the continuous addition of sample points. Bayesian optimization consists of two key processes: Prior Function (PF) and Acquisition Function (AC). The PF uses a Gaussian process to approximate the objective function. The AC was employed to select the subsequent sampling points [49]. In the Bayesian optimization in this study, a random search was performed in five steps, followed by ten iterations of Bayesian optimization. Table 3 lists the optimal parameters obtained after traversing all parameter combinations for All-Day AODES.

Table 3. Optimal parameter combinations for All-Day AODES.

Model	Parameter	Meaning	Value
All-Day AODES	n_estimators	Number of trees	731
	max_depth	Maximum tree depth	41
	min_child_weight	Minimum sample weight sum in child nodes	38.66
	learning_rate	Learning rate	0.031

The Pearson correlation coefficient was employed to examine the correlation between the input variables of the All-Day AODES and AOD. Table 4 presents statistics on the relationship between the input variables of the All-Day AODES and the AOD. The correlation between PM_{2.5} and PM₁₀ in ground air quality data was higher. Similarly, the correlation of BLH and RH in meteorological data also demonstrated high correlation.

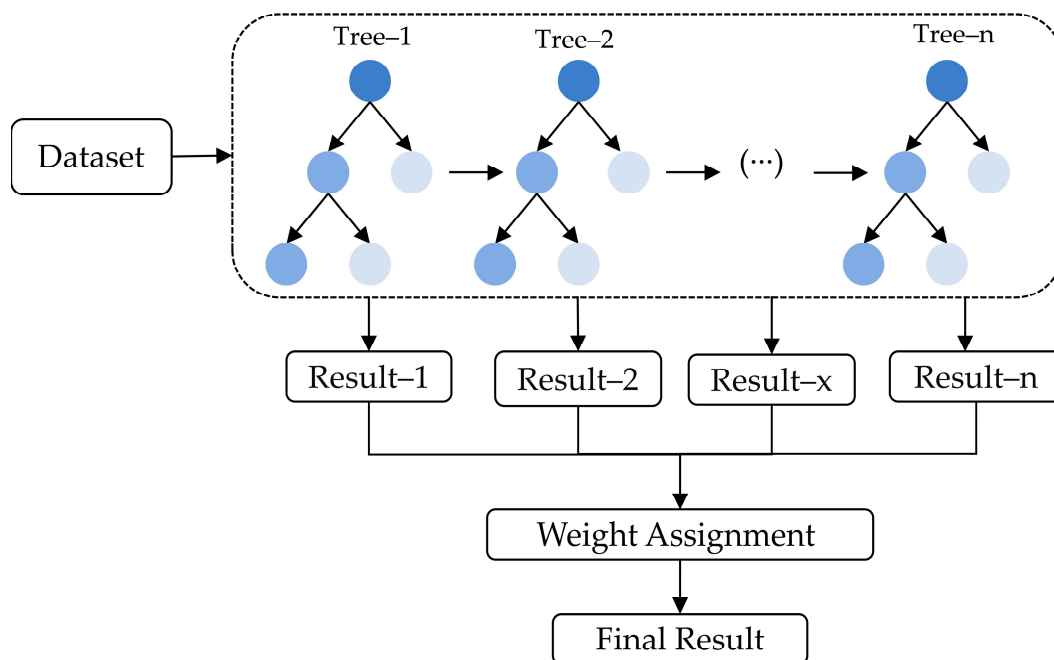


Figure 3. Structure of the XGBoost model.

Table 4. Statistics on the relationship between the input variables of All-Day AODES and AOD.

Variable	AHI AOD		
	Slope	Intercept	Correlation Coefficient
PM _{2.5}	0.006	0.24	0.598
PM ₁₀	0.003	0.217	0.533
SO ₂	0.007	0.373	0.259
NO ₂	0.008	0.274	0.424
O ₃	1.29×10^{-4}	0.454	0.018
BLH	-1.33×10^{-4}	0.627	-0.303
SP	1.01×10^{-5}	-0.539	0.097
T2M	0.004	-0.591	0.101
U10	-0.04	0.497	-0.238
V10	0.037	0.464	0.263
RH	0.008	0.189	0.388

2.2.3. System Model Evaluation

This study validated the model from two perspectives: sample and spatial. It employs two validation methods, as illustrated in Figure 4: sample-based and leave-one-city cross-validation [50,51].

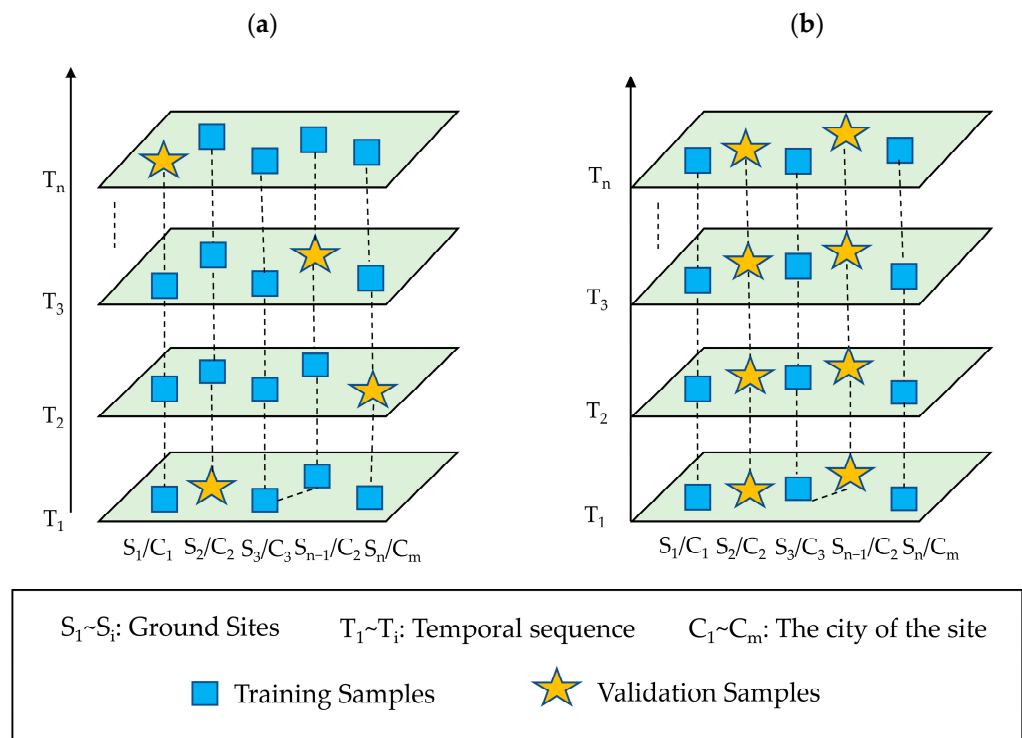


Figure 4. Schematic diagram of two cross-validation methods. (a) The sample-based cross-validation, (b) the leave-one-city cross-validation.

1. Sample-based cross-validation involves partitioning the dataset into ten subsets and performing ten cycles. In each process, nine subsets were used as training data, whereas the remaining subsets served as validation data. The performance of the final trained model was evaluated using a test dataset.
2. Leave-one-city cross-validation involves partitioning the dataset according to the “city” attribute. This study encompasses a total of 13 cities. In each iteration, data from one city served as the validation set, whereas data from the remaining 12 cities constituted the training set. During each iteration, the model was trained on the training set and subsequently evaluated on the test dataset.

After each iteration of the model evaluation process, the model’s performance is determined by calculating the coefficient of determination (R^2) and root mean square error (RMSE) between the predicted and actual values. Equations (1) and (2) represent the formulas for R^2 and RMSE.

$$R^2 = 1 - \frac{\sum_{i=1}^n (AOD_{Ture,i} - AOD_{Estimated,i})}{\sum_{i=1}^n (AOD_{Ture,i} - AOD_{Average})} \quad (1)$$

$$RMSE = \sqrt{\frac{1}{n} \sum_{i=1}^n (AOD_{Ture,i} - AOD_{Estimated,i})^2} \quad (2)$$

3. Results

3.1. Estimation of All-Day AOD

3.1.1. Analytical Comparison of Different Models

Figure 5 presents a scatterplot of the All-Day AODES with sample-based cross-validation. The x -axis represents the AHI AOD and the y -axis represents the estimated AOD. In total, 37,989 validation data points were used. Figure 5 shows that the All-Day

AODES exhibited an R^2 of 0.855, an RMSE of 0.134, and a slope of 0.801, indicating good consistency between the estimated and AHI AOD. However, the All-Day AODES slightly underestimates the AHI AOD.

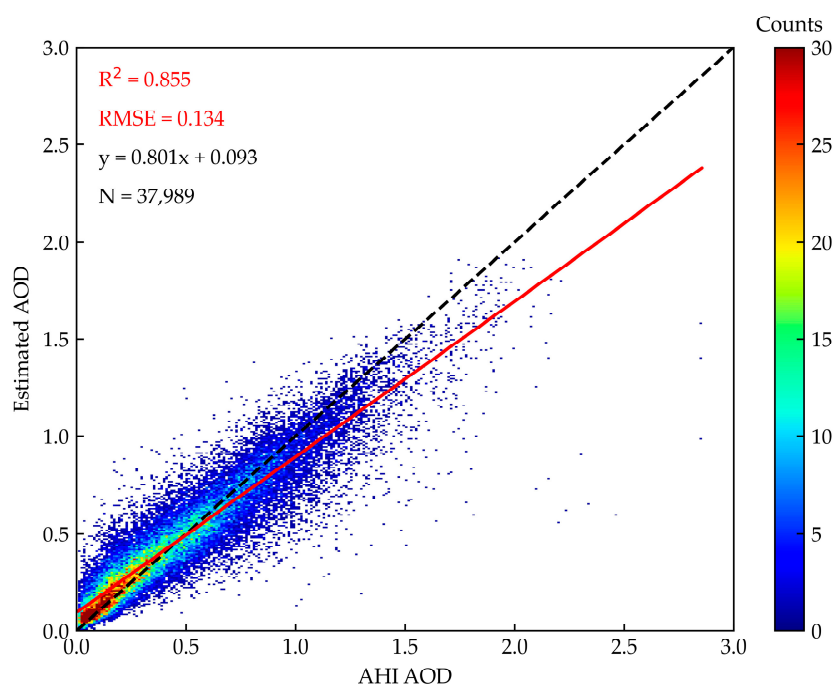


Figure 5. The scatterplot of All-Day AODES. The black dashed line is the 1:1 line and the red solid line is the linear regression line. The information of the model is denoted in the upper-left corner.

The reliability of the model was evaluated by comparing the cross-validation results of the All-Day AODES with those of the Random Forest (RF) and LightGBM (LGBM) models. RF is a decision tree-based ensemble learning method. It constructs numerous decision trees, each trained on distinct random subsets and features [52]. LGBM employs histogram-based learning techniques to identify the most informative split point during each iteration [53]. The primary distinction between the RF, LGBM, and All-Day AODES models is the assignment of weights and the selection of split points. Table 5 provides the optimal hyperparameters for the RF and LGBM. Figure 6 shows the scatterplot fitted to the RF and LGBM models. The RF model exhibited an R^2 of 0.824, RMSE of 0.148, and slope of 0.751. The LGBM showed an R^2 of 0.852, RMSE of 0.135, and slope of 0.815. The All-Day AODES exhibited an R^2 of 0.855, RMSE of 0.134, and slope of 0.801, showing an improvement compared to the RF and LGBM models. The All-Day AODES constructed in this study performed the best among the models, achieving the highest R^2 and lowest RMSE.

Table 5. Optimal hyperparameters of RF and LGBM models.

Model	Parameter	Meaning	Value
RF	n_estimators	Number of trees	429
	max_depth	Maximum tree depth	30
	max_features	Maximum number of features	0.691
	min_samples_split	Minimum number of samples required for internal node redistribution	4
LGBM	n_estimators	Number of trees	967
	max_depth	Maximum tree depth	41
	num_leaves	Number of leaf nodes on a tree	29
	learning_rate	Learning rate	0.119

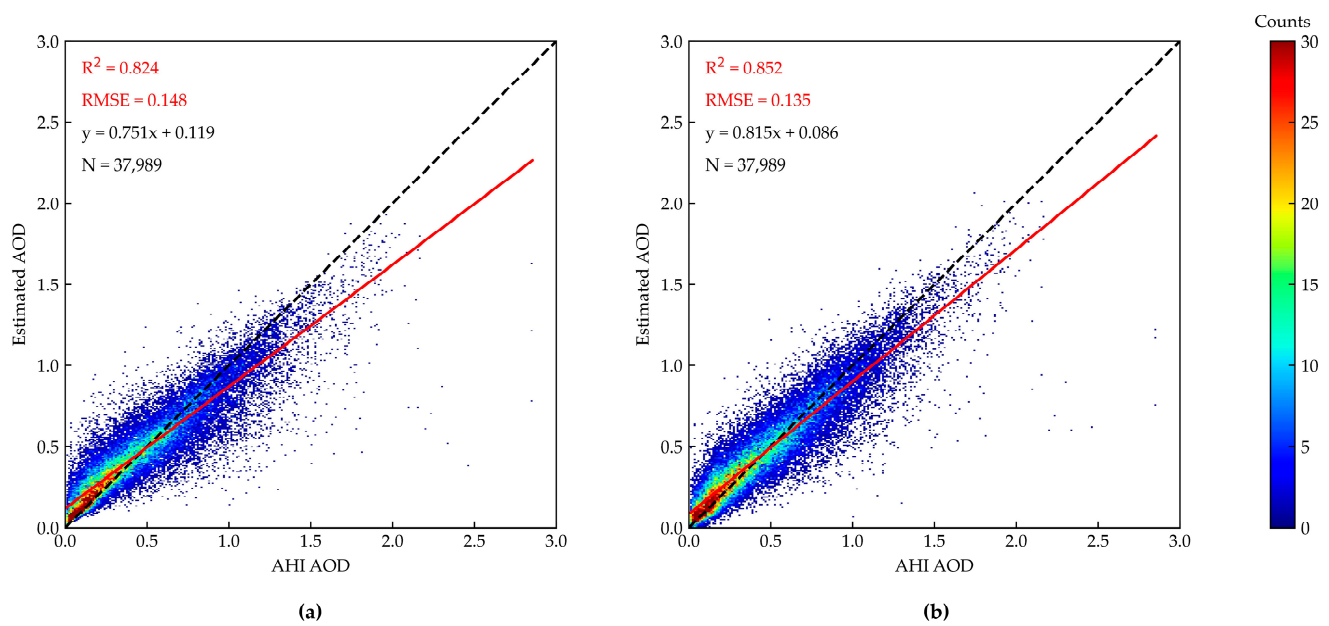


Figure 6. The scatterplot of RF (a) and LGBM (b) models. The black dashed line is the 1:1 line and the red solid line is the linear regression line.

3.1.2. Spatial Extensibility of Different Models

Figures 7 and 8 show the results of the three models (All-Day AODES, RF, LGBM) using the leave-one-city validation for BTH. The x -axis represents the AHI AOD and the y -axis represents the estimated AOD. Figure 7 shows that the All-Day AODES exhibited an R^2 of 0.622, RMSE of 0.216, and slope of 0.621 across the 13 cities. The All-Day AODES showed good spatial extensibility compared to the RF ($R^2 = 0.609$, RMSE = 0.22, and slope = 0.589) and LGBM ($R^2 = 0.607$, RMSE = 0.22, and slope = 0.645).

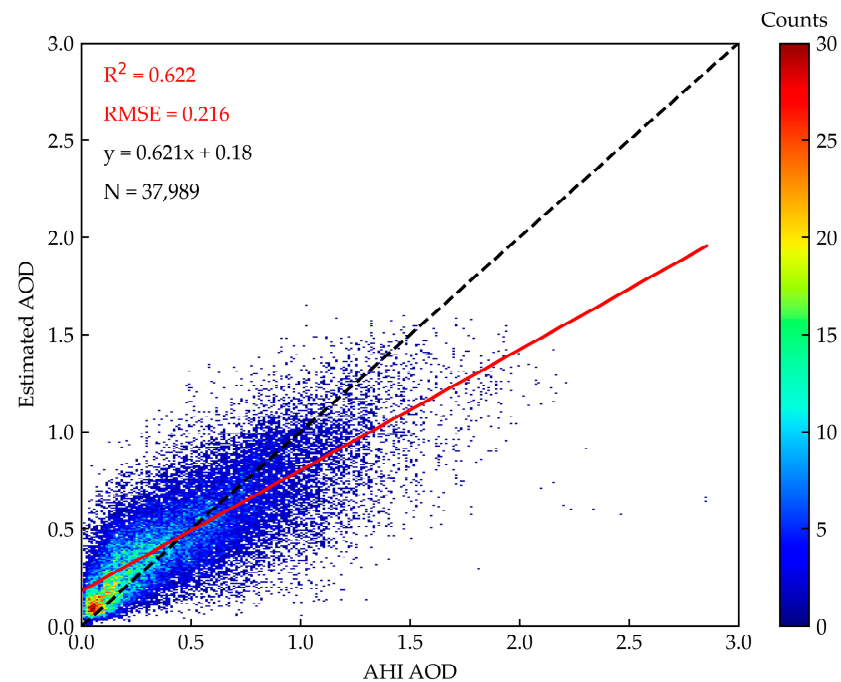


Figure 7. Validation of All-Day AODES. The black dashed line is the 1:1 line and the red solid line is the linear regression line. The information of the model is denoted in the upper-left corner.

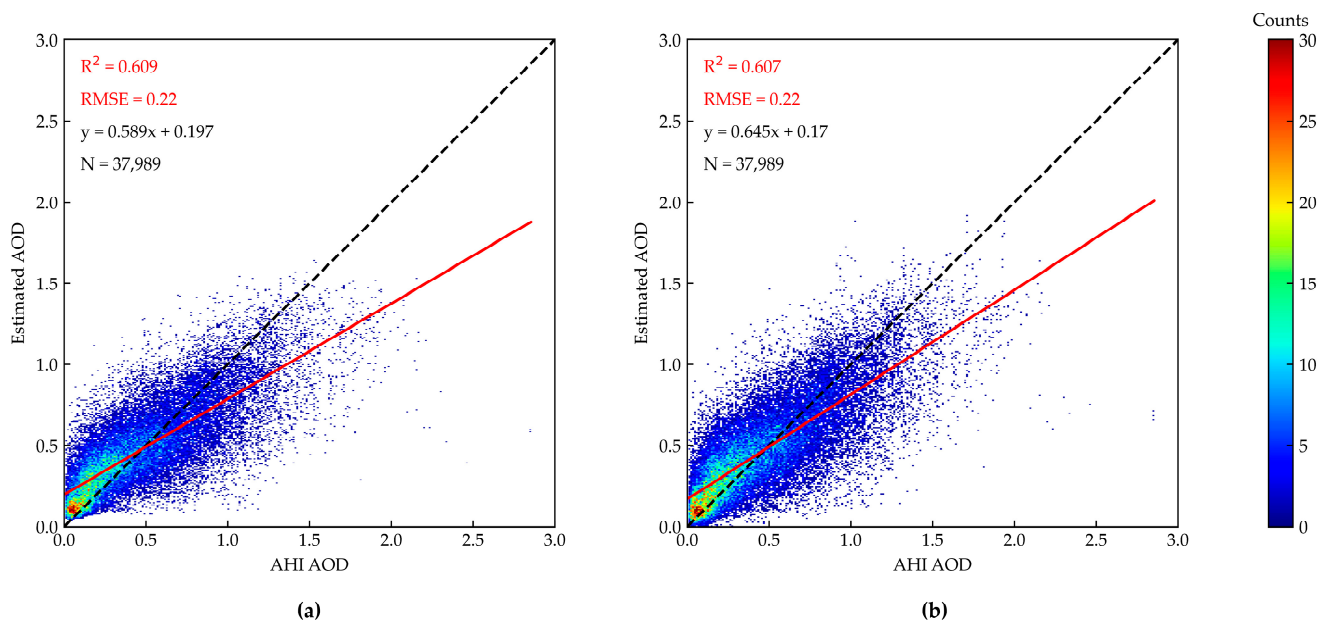


Figure 8. Validation of the RF (a) and LGBM (b) models. The black dashed line is the 1:1 line and the red solid line is the linear regression line.

The R^2 and RMSE were calculated for each validated city and the corresponding estimated sites. Figure 9 shows the spatial extensibility performance of the three models (RF, LGBM, All-Day AODES) using the leave-one-city cross-validation method. Figure 9a–c show multi-radius pie charts with the radius R^2 of the validated city. Green solid circles represent $R^2 = 0.6$ and red dashed circles represent $R^2 = 0.3$. Figure 9a–c show that seven validated cities in each model exhibit an R^2 above 0.6, with none falling below 0.3. Figure 9d–f show the R^2 of each site in the validated cities across all models to further investigate the estimation accuracy of the cities used for validation. A total of 82 estimation sites were distributed across 13 cities. Analysis of Figure 9d–f reveals a difference in the R^2 between the eastern and western cities in BTH, with higher accuracy levels observed at sites located in the eastern cities. Furthermore, the R^2 of southern and northern cities in BTH also demonstrates a disparity, with a higher accuracy observed at sites located in the southern cities. Figure 9g–i show multi-radius pie charts with the radius RMSE of the validated city. The green solid circle indicates RMSE = 0.1 and the red dashed circle indicates RMSE = 0.25. Figure 9g–i show that the RMSE of the 11 validated cities in each model is less than 0.25. Figure 9j–l show the RMSE for each estimated site. Figure 9 shows that the spatial extension method for estimating the AOD using ground air quality and meteorological data exhibited good estimation accuracy, and the estimation error was within acceptable limits.

Table 6 presents the number of sites in the validated cities with an R^2 greater than 0.65 and an RMSE less than 0.2. There were 19 (RF), 21 (LGBM), and 27 (All-Day AODES) sites with an R^2 greater than 0.65, and 17 (RF), 18 (LGBM), and 22 (All-Day AODES) sites with an RMSE less than 0.2. Figure 9 and Table 6 show that the All-Day AODES had better spatial extensibility than the RF and LGBM models. The All-Day AODES has a better spatial performance for verifying rapidly developing cities with a high population density and heavy industrialization. The urban industrial structure of BTH predominantly consists of heavy industry, resulting in frequent pollution incidents in this region. The average annual $PM_{2.5}$ was around $50 \mu\text{g}/\text{m}^3$ in the heavy industrial cities, exemplified by Shijiazhuang and Tangshan, while the average annual $PM_{2.5}$ fell below $35 \mu\text{g}/\text{m}^3$ in the ecological cities, as represented by Zhangjiakou and Qinhuangdao. Consequently, therefore, the All-Day AODES has better spatial extensibility in verifying heavy industrialized cities such as Shijiazhuang and Tangshan. However, Zhangjiakou and Qinhuangdao have limitations compared with other validated cities. These cities may not demonstrate good spatial

extensibility, potentially because of substantial variations in their predominant economic industries and air pollution patterns compared to other cities.

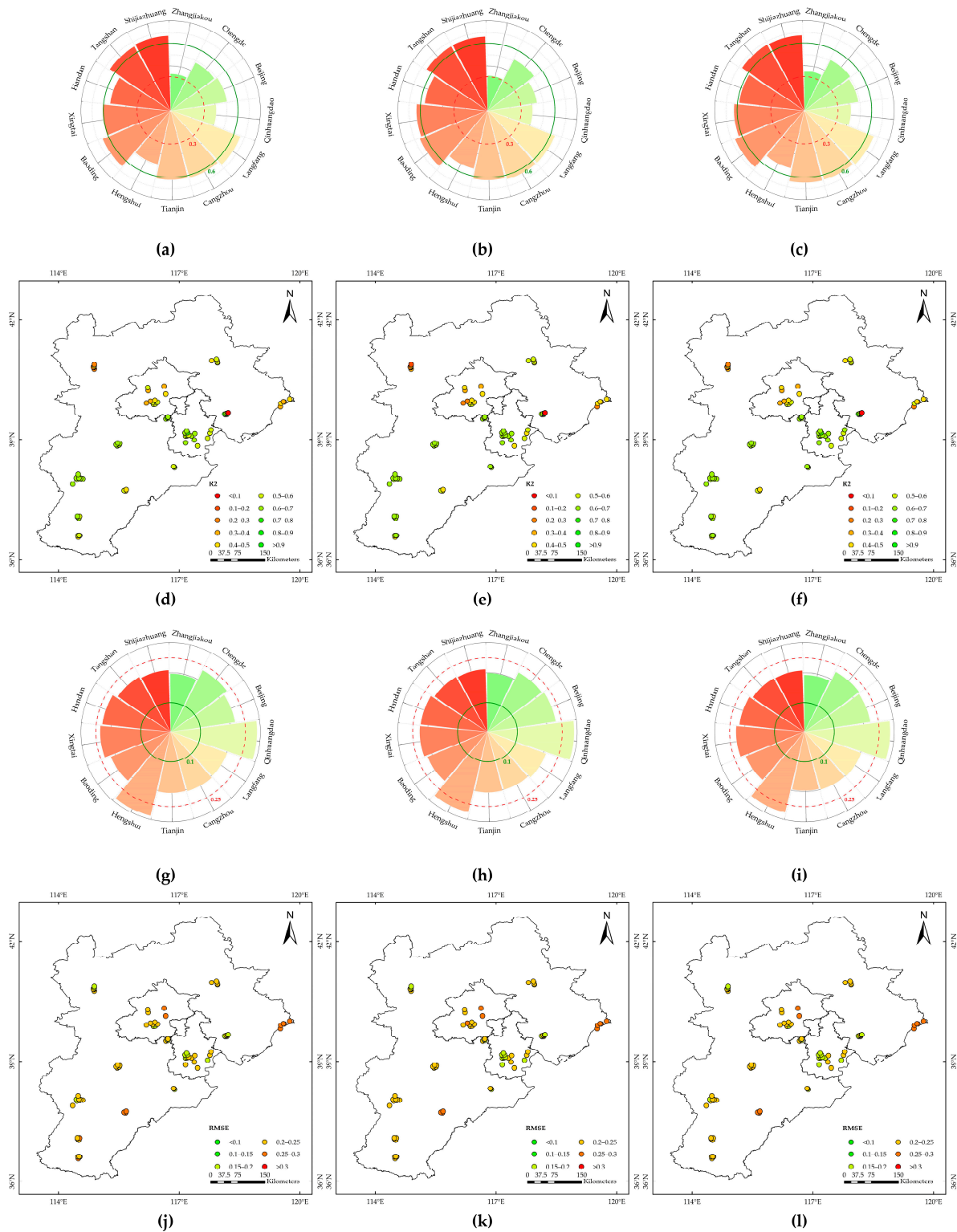


Figure 9. Spatial extensibility of cities and sites based on the leave-one-city cross-validation approach. (a–c): Multi-radius pie charts with radius R^2 of the validated city, (g–i): multi-radius pie charts with radius RMSE. The color of the pie chart from red to green indicates integrated urban pollution from severe to good. (d–f): The R^2 of each site in the validated cities, (j–l): the RMSE of each site.

Table 6. Spatial extensibility of different models in the validated city.

	RF	LGBM	All-Day AODES
$R^2 > 0.65$	19	21	27
RMSE < 0.2	17	18	22

3.2. Verification of All-Day AOD

3.2.1. Comparison with AERONET AOD

To evaluate the estimation accuracy of the model, the Beijing–CAMS in Beijing and Xianghe AERONET site in Hebei province were selected as the validation sites. The AERONET solar photometer records observations at three–minute intervals. The AERONET AOD was filtered by selecting a five–minute window before and after the clock time and the average value within this window was used as the clock data. These clock–time data were used to validate the accuracy of the estimates.

The ground air quality sites of Guanyuan and Xianghe No. 1 Middle School, which are closest to the Beijing–CAMS and Xianghe AERONET sites, were selected as sources for estimating the AOD. They extracted the AOD at the coordinates of the AERONET sites. Time matching was performed between the estimated, AHI, and AERONET AOD.

Figure 10 illustrates the absolute errors between the estimated, AHI, and AERONET AOD. Figure 10a,c show histograms of the absolute error ($X - \text{AERONET}$) between the estimated, AHI, and daytime AERONET AOD. The red solid line represents the normal distribution curve fitted to the absolute error between the estimated and AERONET AOD, whereas the blue dashed line represents the normal distribution curve fitted to the absolute error between the AHI and AERONET AOD. Figure 10a shows that the average absolute error between the estimated and daytime AERONET AOD at the Beijing–CAMS site was 0.0537, with a standard deviation (Std) of 0.2256. The average absolute error between the AHI and AERONET AOD was 0.1289, with an Std of 0.2262. Figure 10c shows that the average absolute error between the estimated and daytime AERONET AOD at the Xianghe site was 0.0384, with an Std of 0.2146. The average absolute error between the AHI and AERONET AOD was 0.0926, with an Std of 0.1873. Figure 10a,c show that the average absolute error between the estimated and AERONET AOD was lower than that of the AHI, in which the average difference between the estimated AOD and AERONET was reduced.

Figure 10e shows histograms of the absolute error between the daytime/nighttime estimated and AERONET AOD. The red solid line represents the normal distribution curve fitted to the absolute error between the daytime estimated and AERONET AOD, whereas the green dashed line represents the normal distribution curve fitted to the absolute error between the nighttime estimated and AERONET AOD. The average absolute error between the nighttime estimated and AERONET AOD was 0.0510, with an Std of 0.1927. The absolute errors between the daytime estimated and AERONET AOD exhibit a more concentrated distribution. The shape of this distribution aligns more closely with a normal distribution. Conversely, for the nighttime AOD, the absolute errors were primarily concentrated within the range of 0.1–0.2.

Figure 10b,d,f show box plots of the absolute error between the estimated and AERONET AOD. The x -axis represents the AERONET AOD and the y -axis represents the absolute error. These boxes represent an error range of 25–75%. The median absolute error is indicated by the solid line at the center of each box. The short lines at the top and bottom of the box plot represent the 10th and 90th percentiles, respectively. The red circles represent the mean of the errors within each interval of size 0.05 of the AOD. The blue diamonds represent the outliers. Figure 10b shows that the estimated AOD at the Beijing–CAMS site changed from overestimation ($\text{AOD} < 0.6$) to underestimation ($\text{AOD} > 0.6$) with an increasing AOD. The dashed line represents the expected uncertainty of the AHI AOD, denoted as $\pm(0.1 + 0.3 \times \text{AOD})$ [54–56]. Figure 10b,d show that 91% of the average absolute errors fall within the expected uncertainty range, indicating that the estimated AOD generally meets the expectations with a slight deviation. Figure 10f shows that 87.5% of the average absolute

errors fall within the expected uncertainty range. It indicates that the estimated AOD is generally as expected, but slightly biased. Notably, an overestimation of the nighttime AOD is observed at low values (AOD < 0.45).

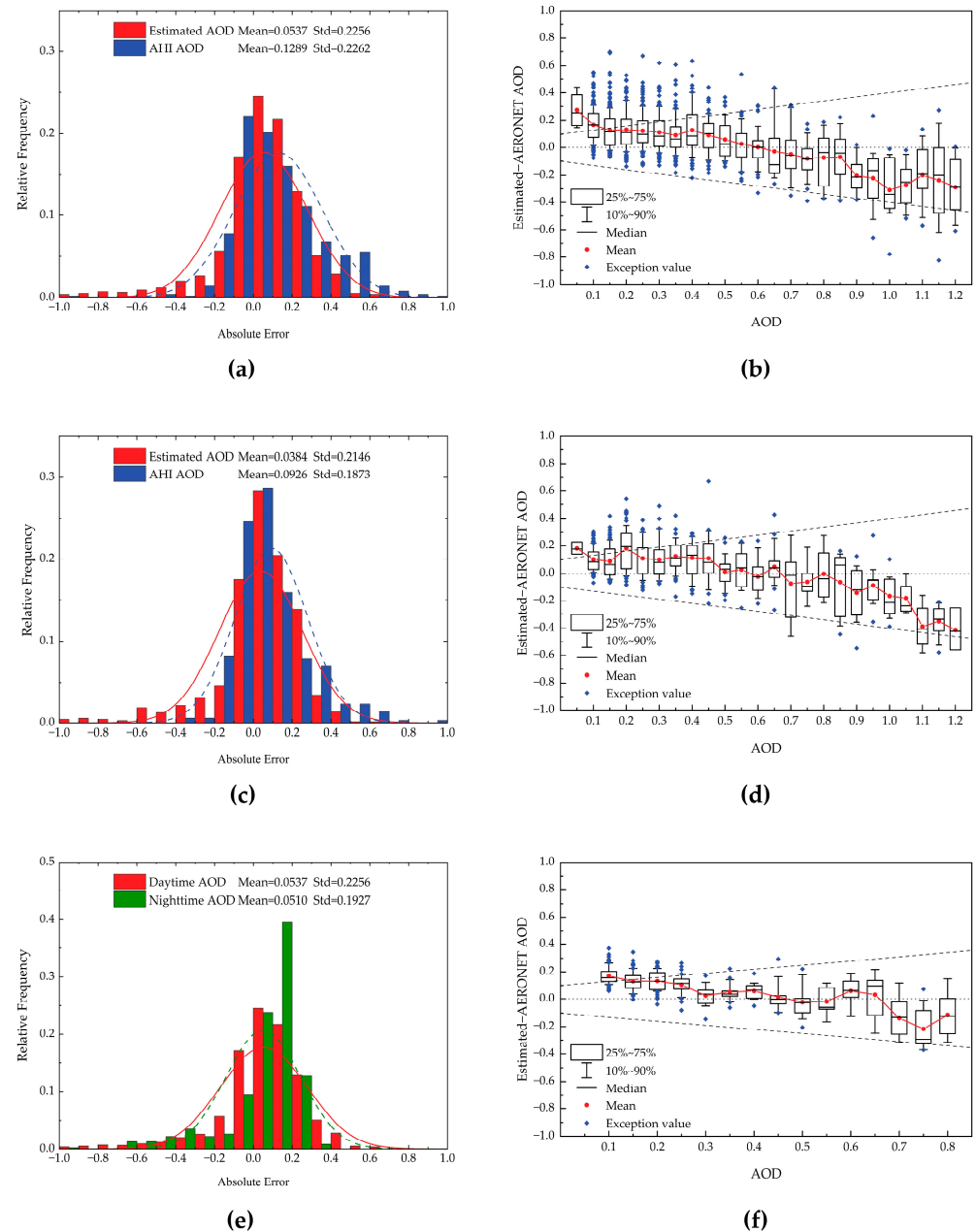


Figure 10. Absolute errors between estimated, AHI, and AERONET AOD. (a,c,e) Histograms and fitted normal distribution curves of the absolute errors. The red solid line represents the normal distribution curve fitted to the absolute error between the estimated and daytime AERONET AOD, the blue dashed line is between the AHI and AERONET AOD, the green dashed line is between the estimated and nighttime AERONET AOD; (b,d,f) box plots of absolute errors of estimated and AERONET AOD. The dashed line is the expected uncertainty in the AHI AOD product (top: $0.1 + 0.3 \times \text{AOD}$; bottom: $-0.1 - 0.3 \times \text{AOD}$). The dotted line in the center is $y = 0$.

3.2.2. Comparison of Time Trends

Figures 11–13 depict the variation in the estimated, AHI, and AERONET AOD. Considering the temporal coverage of the AHI and AERONET, valid data with the time of afternoon (16:00) and next morning (7:00–9:00) in local time were selected. Figure 11 shows

the variation in the three parameters at the Xianghe site from 28 March 2020 22:00 to 30 March 2020 01:00 (UTC). Figures 12 and 13 show the variation in the three parameters at the Beijing–CAMS site from 2 June 2020 22:00 to 4 June 2020 01:00 and from 14 July 2020 22:00 to 16 July 2020 01:00 (UTC), respectively. During the daytime, the trends of the estimated, AHI, and AERONET AOD were similar. From the afternoon to noon of the following day, the variation in the estimated AOD was consistent with the AHI and AERONET production and elimination processes.

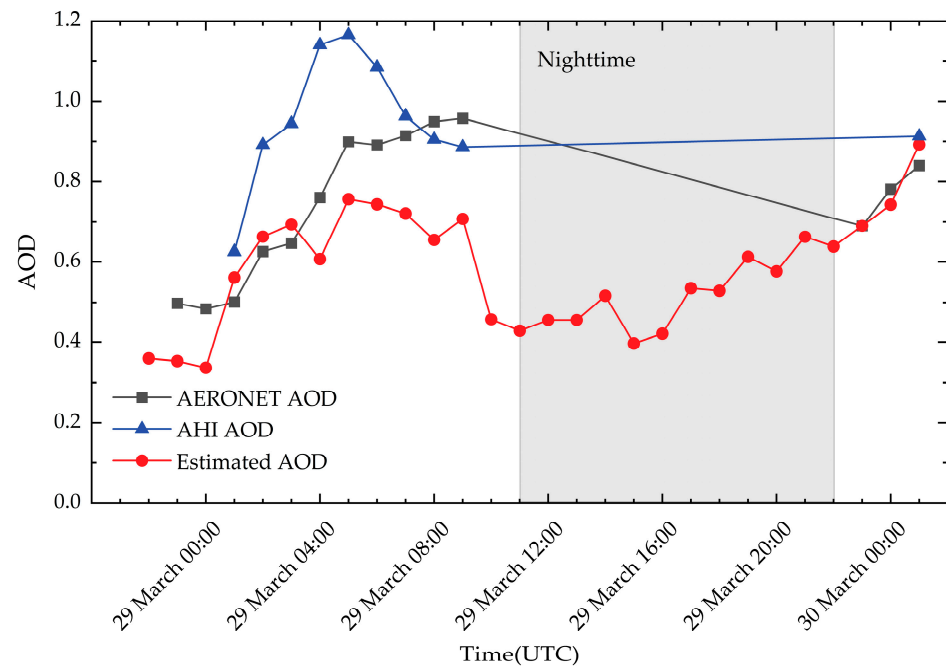


Figure 11. Variation in Xianghe AERONET, AHI, and estimated AOD from 28 March 2020 22:00 to 30 March 2020 01:00.

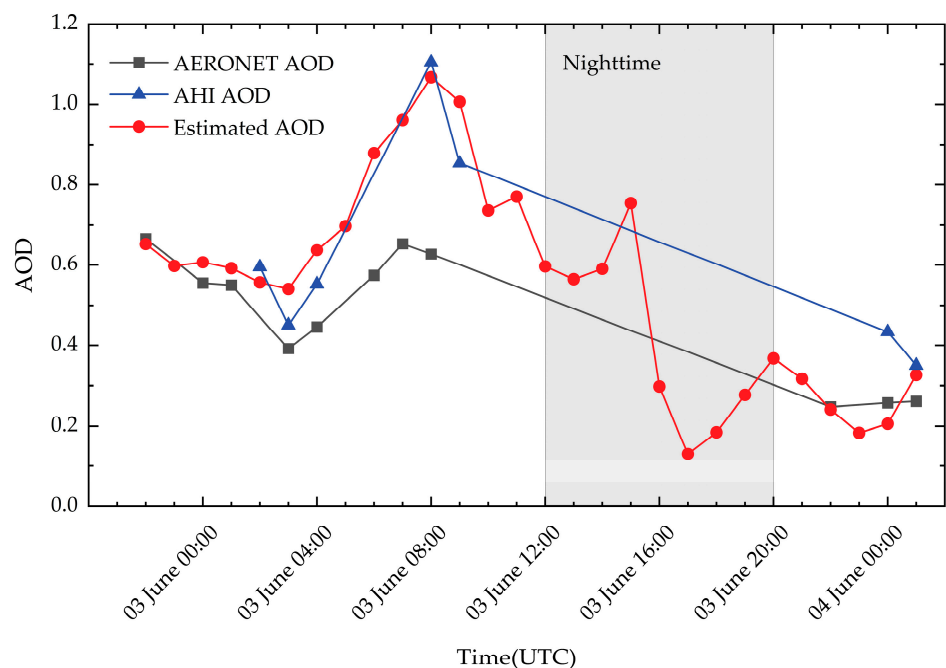


Figure 12. Variation in Beijing–CAMS AERONET, AHI, and estimated AOD from 2 June 2020 22:00 to 4 June 2020 01:00.

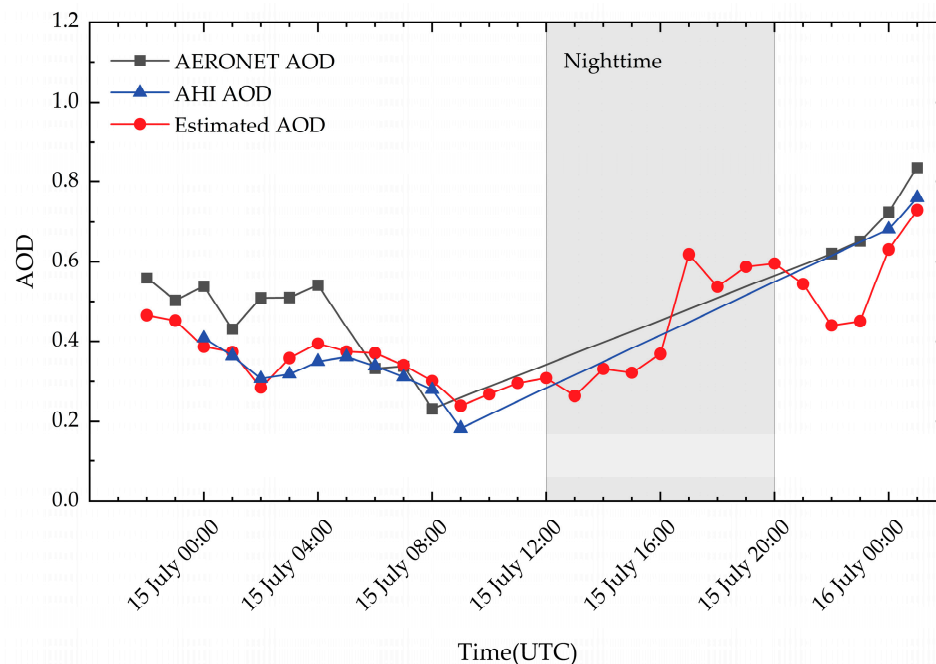


Figure 13. Variation in Beijing–CAMS AERONET, AHI, and estimated AOD from 14 July 2020 22:00 to 16 July 2020 01:00.

The shaded areas in Figures 11–13 represent nighttime periods. The nighttime AOD exhibited a nonlinear and complex trend rather than a simple changing pattern. The complexity of the nighttime AOD is affected by several factors, such as atmospheric stability at night, emissions from terrestrial sources (urban lighting, heating, and industrial production), and changes in meteorological conditions [57]. Together, these factors affect nighttime AOD trends and contribute to their inherent complexity.

3.2.3. Comparison of Spatial Distribution

Figure 14 presents a comparison of the spatial distribution of the true-color image from the Himawari-8, AHI, and estimated AOD in BTH. Considering the characteristics of different seasons, Figure 14 selects the time with snow cover in winter, cloudy in summer, and clear in autumn. Figure 14a shows the true-color image taken by Himawari-8 on 12 January 2020 at 05:00 UTC and Figure 14d shows the distribution of the AHI/estimated AOD during the same period. The spatial distribution of the estimated AOD was similar to that of the AHI, with a significantly higher AOD in the southern region than in the northern region.

Figure 14b,c are true-color images captured by Himawari-8 on 30 May 2020 at 01:00 and 19 September 2020 at 02:00, respectively. Figure 14e,f show the distribution of the AHI/estimated AOD during the same period. In general, the AOD estimated from the All-Day AODES had a spatial distribution similar to that of the AHI. However, the AHI AOD is prone to data gaps owing to clouds, snow, and high surface albedo. In contrast, the All-Day AODES exhibited better stability. The All-Day AODES provides continuous data for different meteorological environments.

Figure 14g–i illustrate the disparities between the estimated and AHI AOD. As depicted in Figure 14g–i, the spatial disparities of the estimated AOD and AHI are minimal. However, in Figure 14g, a significant disparity in the estimated AOD at the southern sites in BTH is observed. This disparity may be attributed to the limited retrieval capabilities of satellites in snow-covered regions, leading to increased disparities in the estimated AOD.

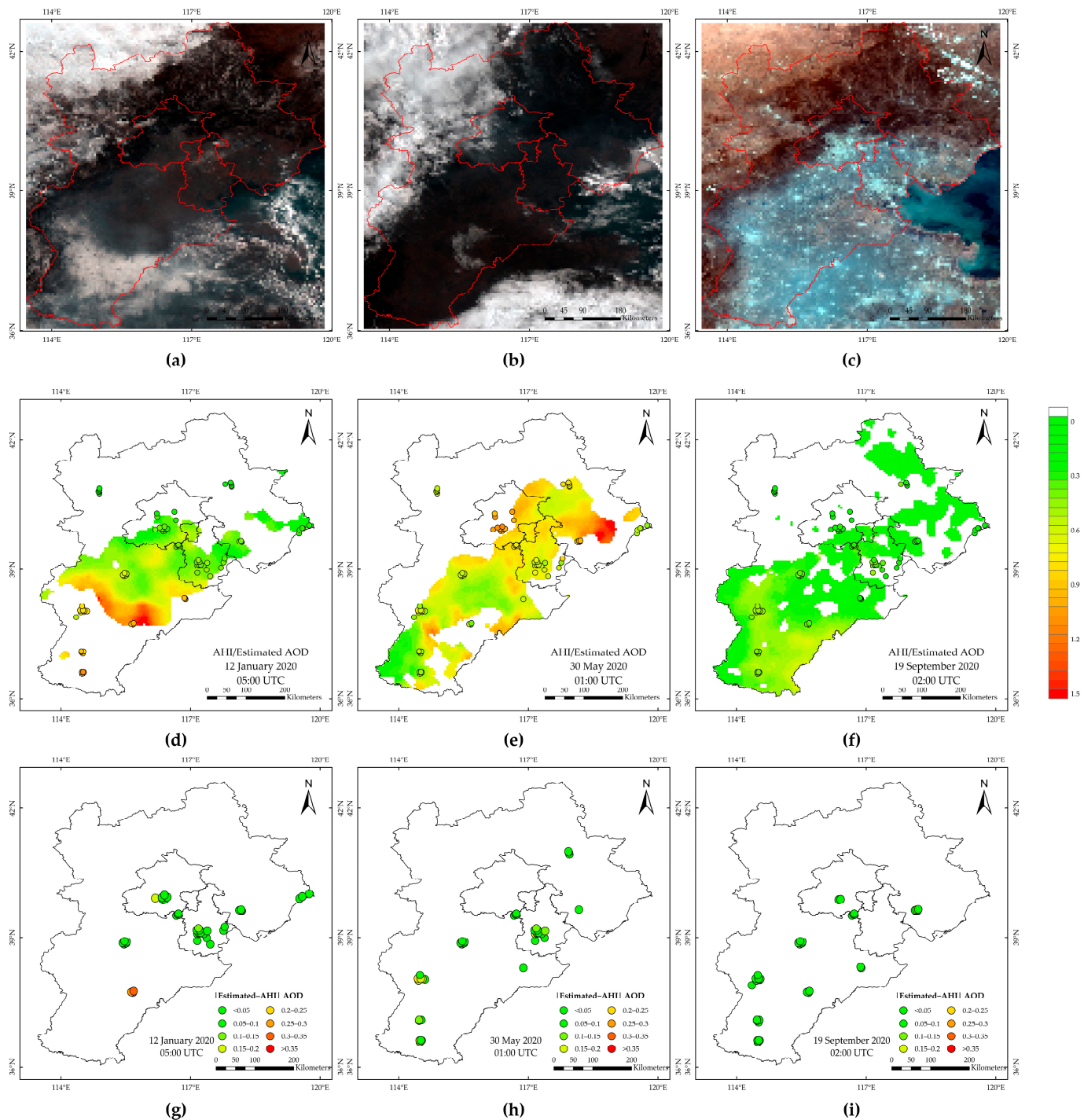


Figure 14. Spatial distribution and disparities of the AHI AOD and estimated AOD in BTH. (a–c): True-color image from Himawari-8; (d–f): the distribution of the AHI/estimated AOD; (g–i): the disparities between estimated and AHI AOD.

3.3. Analysis of All-Day AOD

Figure 15 shows the variation in the hourly mean AOD across each city within BTH. As shown in Figure 15, except for Zhangjiakou and Chengde, all cities displayed similar trends in their hourly mean AOD variations, with an initial increase, followed by a decrease, and eventually leveling off, with peak values typically observed around noon. The divergence in the daytime hourly mean AOD between Zhangjiakou and Chengde is primarily attributed

to significant disparities in air pollution patterns, industrial structures, and population distribution between these two cities and the rest of BTH.

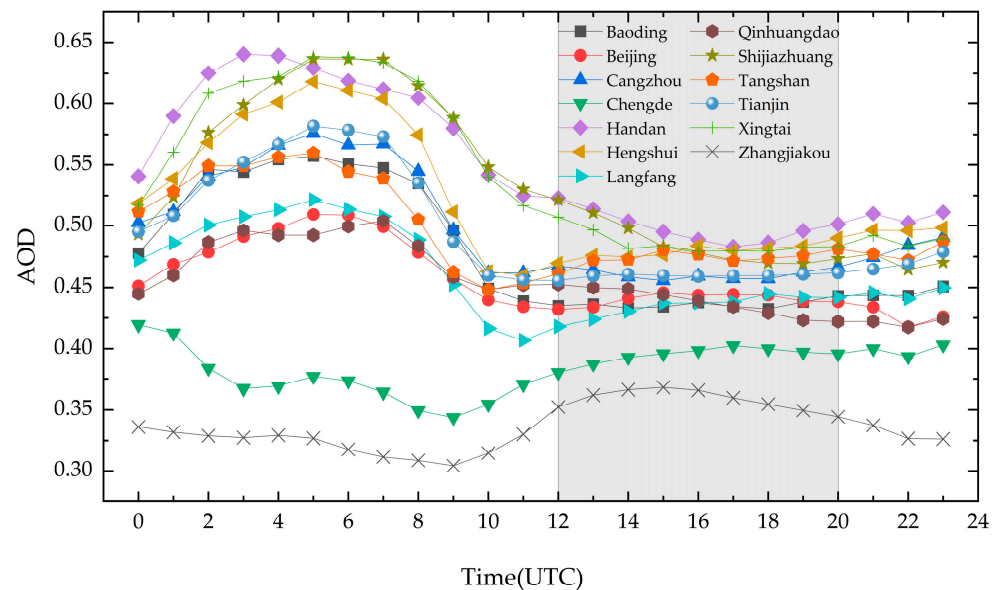


Figure 15. Variation in hourly mean AOD across each city within BTH.

The shaded region in Figure 15 represents nighttime hours. It is evident from this shaded region that the hourly average AOD exhibited a smoother change during the nighttime than during the daytime. There are two main reasons for this phenomenon:

1. Reduction in human activity, with reductions in transportation, industrial production, and other nighttime activities leading to a decrease in airborne particulate emissions.
2. Relative weakening of atmospheric turbulence during the nighttime, which slows the vertical movement of air, diminishing the diffusion and mixing of aerosols.

4. Discussion

This study proposed a method for estimating the AOD throughout the day using ground air quality and meteorological data. The proposed method achieved an All-Day hourly estimated AOD for BTH. Using ground air quality data ($PM_{2.5}$, PM_{10} , SO_2 , NO_2 , and O_3) and meteorological data (BLH, SP, T2M, U10, V10, and RH), we constructed three AOD models (RF, LGBM, All-Day AODES) to estimate the AOD throughout the day and night. In a comparison of model performance and spatial extensibility with the RF and LGBM models, the All-Day AODES showed a sample-based cross-validation accuracy R^2 of 0.855, an RMSE value of 0.134, and a slope of 0.801. The All-Day AODES achieved an accuracy R^2 of 0.622, RMSE of 0.216, and slope of 0.621 using a leave-one-city cross-validation. The All-Day AODES outperformed both the RF and LGBM models in terms of estimation accuracy and spatial extensibility. However, the validation of the spatial extensibility of the model was unsatisfactory for Zhangjiakou and Qinhuangdao. This can be attributed to the significant differences in air pollution patterns between these and other cities. Most cities in BTH have industrial structures mainly based on heavy industries. Therefore, large amounts of industrial emissions have worsened the air pollution. In contrast, Zhangjiakou and Qinhuangdao, which are crucial ecological conservation areas, maintained good air quality. The annual average $PM_{2.5}$ concentration in Zhangjiakou is $23 \mu\text{g}/\text{m}^3$, compared to $34 \mu\text{g}/\text{m}^3$ in Qinhuangdao. Owing to the significant atmospheric differences among the cities in BTH, cross-validation of the model by excluding one city shows that the model designed to capture the characteristics of industrial cities' air lacks spatial extensibility when adapted to cities with better air quality.

To further verify the accuracy of the AOD estimation, a comprehensive analysis was conducted to explore both temporal and spatial aspects. The results showed that, in

terms of the temporal dimension, the estimated AOD was consistent with the trends of the AHI and AERONET AOD measured data during the daytime. The absolute errors of the estimated AOD relative to the AERONET sites were relatively small compared to those of the AHI AOD. The estimated AOD was closer to the AERONET than to the AHI. Furthermore, when satellite or ground monitoring values are missing during the day, the estimated AOD improves the temporal coverage and represents temporal variations more effectively. Simultaneously, the estimated AOD captured complex nighttime AOD variations. These nighttime changes in the estimated AOD not only coincided with the generation and elimination processes observed in the AHI AOD and AERONET AOD but also described the hourly resolution fluctuations in the nighttime AOD. In addition, the estimated nighttime AOD showed non-monotonic variation. Complex variations in the nighttime AOD hinder the accurate assessment of indirect aerosol radiative forcing effects and their impact on climate change. Therefore, the estimated AOD from the All-Day AODES partially fills the gap in high temporal resolution nighttime AOD monitoring, thus providing valuable data support for nighttime aerosol research. The spatial distribution of the estimated AOD was similar to that of the AHI AOD. Notably, the All-Day AODES can still provide accurate AOD data even when satellite AOD data are missing due to clouds, snow, and high surface albedo cover. Reasonable use of the estimated AOD can fill gaps in the satellite AOD data, thereby improving aerosol monitoring and increasing spatial coverage.

The estimated AOD of the All-Day AODES showed improved temporal completeness compared to those of the AHI and AERONET AOD. In 2020, the All-Day AODES generated 648,850 data points with up to 90% temporal coverage. Figure 16 shows the temporal completeness of the AERONET, AHI, and estimated AOD from the All-Day AODES for two AERONET sites in 2020. The estimated AOD had a data completeness of up to 80% per hour. Compared to the AERONET and AHI AOD, the temporal completeness of the estimated AOD from the All-Day AODES was significantly improved. It is worth noting that the All-Day AODES provided data throughout the night, whereas the AERONET AOD and AHI AOD did not.

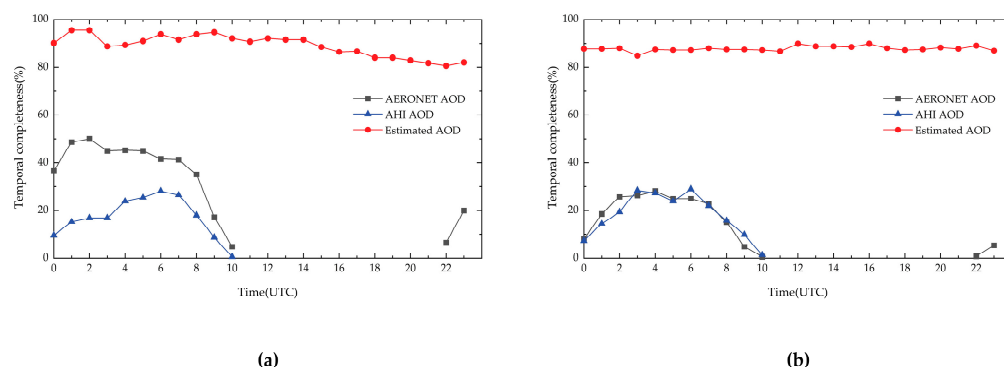


Figure 16. Temporal completeness of AERONET AOD, AHI AOD, and estimated AOD in 2020: (a) Beijing–CAMS AERONET site and (b) Xianghe AERONET site.

Although this study proposed a more advanced model for monitoring the AOD throughout the day, it is necessary to realize its inherent limitations. Firstly, the feasibility of the All-Day AODES was demonstrated only through experiments using ground air quality sites in BTH. However, enhancing the experiment with a larger air quality monitoring network and more ground air quality sites could produce more accurate and refined AOD data. Secondly, currently common parameters were used. However, other factors such as aerosol type, aerosol chemistry, surface type, population, and economy may have affected the experimental results. Expanding the range of parameters can improve the accuracy of the model. Thirdly, given that this study utilizes daytime AOD for model construction, it may not sufficiently account for the daily variations in ground air quality and meteorological data. Future advancements in AERONET and lunar photometer algorithms would

enable the acquisition of nighttime aerosol properties. Finally, the All-Day AODES relies on ground air quality data; therefore, the estimated AOD is point data. To further explore the aerosol distribution and trends, it is beneficial to use spatial interpolation techniques or satellite data to obtain All-Day aerosol data with continuous spatial coverage.

5. Conclusions

The All-Day AODES was constructed using ground air quality data, meteorological data, and daytime satellite AOD data to estimate the hourly AOD throughout the day in BTH. Following the validation, several conclusions were drawn.

1. The All-Day AODES achieved an R^2 of 0.855, RMSE of 0.134, and slope of 0.801 based on sample-based cross-validation. Additionally, the All-Day AODES demonstrated commendable spatial extensibility based on leave-one-city cross-validation, achieving an R^2 of 0.622, RMSE of 0.216, and slope of 0.621. In this study, the All-Day AODES outperformed the RF and LGBM under two different cross-validations. The All-Day AODES has a higher estimation accuracy and fitting ability, and can better capture the differences between different cities.
2. The average absolute error between the estimated and daytime AERONET AOD at the Beijing-CAMS site was 0.0537 with an Std of 0.2256; the average absolute error between the estimated and nighttime AERONET AOD at the Beijing-CAMS site was 0.0510, with an Std of 0.1927; and the average absolute error between the estimated and daytime AERONET AOD at the Xianghe site was 0.0384 with an Std of 0.2146. The average disparities between the estimated AOD and AERONET are minimal. A comparison between the estimated, AHI, and AERONET AOD showed that the average absolute errors between the estimated and AERONET AOD were smaller than those between the AHI and AERONET AOD. The estimated value was closer to the AERONET AOD than to the AHI AOD. In addition, 91% of the average absolute errors of the daytime estimated values were within the uncertainty range of the AHI AOD, 87.5% of the average absolute errors of the nighttime estimated AOD fall within the expected uncertainty range.
3. The estimated AOD of the All-Day AODES shows spatial and temporal trends similar to those of the AERONET and AHI and can more accurately reflect the nighttime AOD trend.
4. The All-Day AODES showed an enhanced level of temporal completeness. This compensates for the absence of satellite AOD data and furnishes hourly estimated nighttime AOD.

In conclusion, the All-Day AODES implements continuous monitoring of the AOD in BTH and addresses the lack of high temporal resolution monitoring of the AOD during nighttime. Continuous estimation of the AOD offers valuable data for evaluating the impact of aerosol radiation and climate change.

Author Contributions: Conceptualization, methodology, validation, formal analysis, and data curation, W.Z. and S.L.; writing—original draft preparation, S.L.; writing—review and editing, all authors; investigation, X.C.; supervision, X.G. and T.Y.; funding acquisition, W.Z. and S.L.; and project administration, X.M. All authors have read and agreed to the published version of the manuscript.

Funding: This research was funded by the Major Project of High-Resolution Earth Observation System, Nos. 30-Y60B01-9003-22/23 and 30-Y30F06-9003-20/22; North China Institute of Aerospace Engineering Foundation of Doctoral Research, No. BKY-2021-31; Science and Technology Research Projects of Higher Education Institutions in Hebei Province, No. ZD2021303; North China Institute of Aerospace Engineering's University-level Innovation Project, No. YKY-2023-78; and Hebei Province Graduate Student Innovation Ability Training Funding Project, No. CXZZSS2024141.

Data Availability Statement: The data in this article can be found online at <https://mega.nz/folder/ly9hTCLi#uuX3Z5VWsExmfKxPm0WB7w> (accessed on 3 February 2024).

Acknowledgments: We appreciate the support of the China National Environmental Monitoring Center in providing ground air quality data, the European Centre for Medium-Range Weather Forecasts in providing reanalysis meteorological data, the Aerosol Robotic Network in providing AERONET AOD, and the Japan Aerospace Exploration Agency in providing AHI AOD. In addition, we sincerely appreciate all the anonymous reviewers for their excellent comments and efforts.

Conflicts of Interest: The authors declare no conflicts of interest.

References

- Gras, J.L. AEROSOLS | Climatology of Tropospheric Aerosols. In *Encyclopedia of Atmospheric Sciences*; Elsevier: Amsterdam, The Netherlands, 2003; pp. 13–20.
- IPCC. *Climate Change 2007: Mitigation of Climate Change*; Cambridge University Press: Cambridge, UK, 2007; ISBN 978-0-511-54601-3.
- Kaufman, Y.J.; Tanré, D.; Boucher, O. A Satellite View of Aerosols in the Climate System. *Nature* **2002**, *419*, 215–223. [[CrossRef](#)] [[PubMed](#)]
- Forster, P.; Ramaswamy, V.; Artaxo, P.; Berntsen, T.; Betts, R.; Fahey, D.W.; Haywood, J.; Lean, J.; Lowe, D.C.; Myhre, G.; et al. Changes in Atmospheric Constituents and in Radiative Forcing. In *Climate Change 2007: The Physical Science Basis. Contribution of Working Group I to the 4th Assessment Report of the Intergovernmental Panel on Climate Change*; Solomon, S., Qin, D., Manning, M., Chen, Z., Marquis, M., Averyt, K.B., Tignor, M., Miller, H.L., Eds.; Cambridge University Press: Cambridge, UK; New York, NY, USA, 2007.
- Myhre, G. Consistency Between Satellite-Derived and Modeled Estimates of the Direct Aerosol Effect. *Science* **2009**, *325*, 187–190. [[CrossRef](#)] [[PubMed](#)]
- Wu, D.; Tie, X.; Li, C.; Ying, Z.; Kai-Hon Lau, A.; Huang, J.; Deng, X.; Bi, X. An Extremely Low Visibility Event over the Guangzhou Region: A Case Study. *Atmos. Environ.* **2005**, *39*, 6568–6577. [[CrossRef](#)]
- Moody, J.L.; Keene, W.C.; Cooper, O.R.; Voss, K.J.; Aryal, R.; Eckhardt, S.; Holben, B.; Maben, J.R.; Izaguirre, M.A.; Galloway, J.N. Flow Climatology for Physicochemical Properties of Dichotomous Aerosol over the Western North Atlantic Ocean at Bermuda. *Atmos. Chem. Phys.* **2014**, *14*, 691–717. [[CrossRef](#)]
- Tzani, C.; Varotsos, C.; Ferm, M.; Christodoulakis, J.; Assimakopoulos, M.N.; Efthymiou, C. Nitric Acid and Particulate Matter Measurements at Athens, Greece, in Connection with Corrosion Studies. *Atmos. Chem. Phys.* **2009**, *9*, 8309–8316. [[CrossRef](#)]
- Tzani, C.; Varotsos, C.; Christodoulakis, J.; Tidblad, J.; Ferm, M.; Ionescu, A.; Lefevre, R.-A.; Theodorakopoulou, K.; Kreislova, K. On the Corrosion and Soiling Effects on Materials by Air Pollution in Athens, Greece. *Atmos. Chem. Phys.* **2011**, *11*, 12039–12048. [[CrossRef](#)]
- Von Der Weiden-Reinmüller, S.-L.; Drewnick, F.; Crippa, M.; Prévôt, A.S.H.; Meleux, F.; Baltensperger, U.; Beekmann, M.; Borrmann, S. Application of Mobile Aerosol and Trace Gas Measurements for the Investigation of Megacity Air Pollution Emissions: The Paris Metropolitan Area. *Atmos. Meas. Tech.* **2014**, *7*, 279–299. [[CrossRef](#)]
- Al-Saadi, J.; Szykman, J.; Pierce, R.B.; Kittaka, C.; Neil, D.; Chu, D.A.; Remer, L.; Gumley, L.; Prins, E.; Weinstock, L.; et al. Improving National Air Quality Forecasts with Satellite Aerosol Observations. *Bull. Am. Meteorol. Soc.* **2005**, *86*, 1249–1262. [[CrossRef](#)]
- Ho, H.C.; Wong, M.S.; Yang, L.; Shi, W.; Yang, J.; Bilal, M.; Chan, T.-C. Spatiotemporal Influence of Temperature, Air Quality, and Urban Environment on Cause-Specific Mortality during Hazy Days. *Environ. Int.* **2018**, *112*, 10–22. [[CrossRef](#)] [[PubMed](#)]
- Mishchenko, M.I.; Geogdzhayev, I.V.; Cairns, B.; Carlson, B.E.; Chowdhary, J.; Laci, A.A.; Liu, L.; Rossow, W.B.; Travis, L.D. Past, Present, and Future of Global Aerosol Climatologies Derived from Satellite Observations: A Perspective. *J. Quant. Spectrosc. Radiat. Transf.* **2007**, *106*, 325–347. [[CrossRef](#)]
- Varotsos, C.; Ondov, J.; Tzani, C.; Öztürk, F.; Nelson, M.; Ke, H.; Christodoulakis, J. An Observational Study of the Atmospheric Ultra-Fine Particle Dynamics. *Atmos. Environ.* **2012**, *59*, 312–319. [[CrossRef](#)]
- Doyle, M.; Dorling, S. Satellite and Ground Based Monitoring of Aerosol Plumes. In *Urban Air Quality—Recent Advances*; Sokhi, R.S., Bartzi, J.G., Eds.; Springer: Dordrecht, The Netherlands, 2002; pp. 615–629. ISBN 978-94-010-3935-2.
- Barreto, Á.; Cuevas, E.; Granados-Muñoz, M.-J.; Alados-Arboledas, L.; Romero, P.M.; Gröbner, J.; Kouremeti, N.; Almansa, A.F.; Stone, T.; Toledano, C.; et al. The New Sun-Sky-Lunar Cimel CE318-T Multiband Photometer—A Comprehensive Performance Evaluation. *Atmos. Meas. Tech.* **2016**, *9*, 631–654. [[CrossRef](#)]
- De Leeuw, G.; Holzer-Popp, T.; Bevan, S.; Davies, W.H.; Desclotres, J.; Grainger, R.G.; Griesfeller, J.; Heckel, A.; Kinne, S.; Klüser, L.; et al. Evaluation of Seven European Aerosol Optical Depth Retrieval Algorithms for Climate Analysis. *Remote Sens. Environ.* **2015**, *162*, 295–315. [[CrossRef](#)]
- Li, C.F.; Dai, Y.Y.; Liu, F.; Zhao, J.J. Inversion of Aerosol Optical Depth Based on MODIS Remote Sensor. *Appl. Mech. Mater.* **2015**, *738–739*, 209–212. [[CrossRef](#)]
- Hsu, N.C.; Jeong, M.-J.; Bettenhausen, C.; Sayer, A.M.; Hansell, R.; Seftor, C.S.; Huang, J.; Tsay, S.-C. Enhanced Deep Blue Aerosol Retrieval Algorithm: The Second Generation. *J. Geophys. Res. Atmos.* **2013**, *118*, 9296–9315. [[CrossRef](#)]
- Han, J.; Tao, Z.; Xie, Y.; Li, H.; Liu, Q.; Guan, X. A Novel Radiometric Cross-Calibration of GF-6/WFV with MODIS at the Dunhuang Radiometric Calibration Site. *IEEE J. Sel. Top. Appl. Earth Obs. Remote Sens.* **2021**, *14*, 1645–1653. [[CrossRef](#)]

21. Han, J.; Tao, Z.; Xie, Y.; Li, H.; Guan, X.; Yi, H.; Shi, T.; Wang, G. Radiometric Cross-Calibration of GF-6/WFV Sensor Using MODIS Images with Different BRDF Models. *IEEE Trans. Geosci. Remote Sens.* **2022**, *60*, 5409311. [[CrossRef](#)]
22. Zhang, J.; Reid, J.S.; Miller, S.D.; Turk, F.J. Strategy for Studying Nocturnal Aerosol Optical Depth Using Artificial Lights. *Int. J. Remote Sens.* **2008**, *29*, 4599–4613. [[CrossRef](#)]
23. Johnson, R.S.; Zhang, J.; Hyer, E.J.; Miller, S.D.; Reid, J.S. Preliminary Investigations toward Nighttime Aerosol Optical Depth Retrievals from the VIIRS Day/Night Band. *Atmos. Meas. Tech.* **2013**, *6*, 1245–1255. [[CrossRef](#)]
24. Jiang, M.; Chen, L.; He, Y.; Hu, X.; Liu, M.; Zhang, P. Nighttime aerosol optical depth retrievals from VIIRS day/night band data. *Natl. Remote Sens. Bull.* **2022**, *26*, 493–504. [[CrossRef](#)]
25. Li, H.; Hu, S.; Ma, S.; Tan, Z.; Ai, W.; Yan, W. Retrieving Nighttime Aerosol Optical Depth Using Combined Measurements of Satellite Low Light Channels and Ground-Based Integrating Spheres. *Int. J. Remote Sens.* **2022**, 1–13. [[CrossRef](#)]
26. Giles, D.M.; Sinyuk, A.; Sorokin, M.G.; Schafer, J.S.; Smirnov, A.; Slutsker, I.; Eck, T.F.; Holben, B.N.; Lewis, J.R.; Campbell, J.R.; et al. Advancements in the Aerosol Robotic Network (AERONET) Version 3 Database—Automated near-Real-Time Quality Control Algorithm with Improved Cloud Screening for Sun Photometer Aerosol Optical Depth (AOD) Measurements. *Atmos. Meas. Tech.* **2019**, *12*, 169–209. [[CrossRef](#)]
27. Burton, S.P.; Ferrare, R.A.; Hostetler, C.A.; Hair, J.W.; Rogers, R.R.; Obland, M.D.; Butler, C.F.; Cook, A.L.; Harper, D.B.; Froyd, K.D. Aerosol Classification Using Airborne High Spectral Resolution Lidar Measurements—Methodology and Examples. *Atmos. Meas. Tech.* **2012**, *5*, 73–98. [[CrossRef](#)]
28. Kolmonen, P.; Sogacheva, L.; Virtanen, T.H.; De Leeuw, G.; Kulmala, M. The ADV/ASV AATSR Aerosol Retrieval Algorithm: Current Status and Presentation of a Full-Mission AOD Dataset. *Int. J. Digit. Earth* **2016**, *9*, 545–561. [[CrossRef](#)]
29. Jalal, K.A.; Asmat, A.; Ahmad, N. Aerosol Optical Depth (AOD) Retrieval Method Using MODIS. In Proceedings of the 2015 International Conference on Space Science and Communication (IconSpace), Langkawi, Malaysia, 10–12 August 2015; IEEE: Piscataway, NJ, USA, 2015; pp. 370–374.
30. Miller, S.; Straka, W.; Mills, S.; Elvidge, C.; Lee, T.; Solbrig, J.; Walther, A.; Heidinger, A.; Weiss, S. Illuminating the Capabilities of the Suomi National Polar-Orbiting Partnership (NPP) Visible Infrared Imaging Radiometer Suite (VIIRS) Day/Night Band. *Remote Sens.* **2013**, *5*, 6717–6766. [[CrossRef](#)]
31. Yang, F.; Wang, Y.; Tao, J.; Wang, Z.; Fan, M.; De Leeuw, G.; Chen, L. Preliminary Investigation of a New AHI Aerosol Optical Depth (AOD) Retrieval Algorithm and Evaluation with Multiple Source AOD Measurements in China. *Remote Sens.* **2018**, *10*, 748. [[CrossRef](#)]
32. Kikuchi, M.; Murakami, H.; Suzuki, K.; Nagao, T.M.; Higurashi, A. Improved Hourly Estimates of Aerosol Optical Thickness Using Spatiotemporal Variability Derived From Himawari-8 Geostationary Satellite. *IEEE Trans. Geosci. Remote Sens.* **2018**, *56*, 3442–3455. [[CrossRef](#)]
33. Zheng, Y.; Che, H.; Yang, L.; Chen, J.; Wang, Y.; Xia, X.; Zhao, H.; Wang, H.; Wang, D.; Gui, K.; et al. Optical and Radiative Properties of Aerosols during a Severe Haze Episode over the North China Plain in December 2016. *J. Meteorol. Res.* **2017**, *31*, 1045–1061. [[CrossRef](#)]
34. Miller, S.D.; Combs, C.L.; Kidder, S.Q.; Lee, T.F. Assessing Moonlight Availability for Nighttime Environmental Applications by Low-Light Visible Polar-Orbiting Satellite Sensors. *J. Atmos. Ocean. Technol.* **2012**, *29*, 538–557. [[CrossRef](#)]
35. Giles, D.M.; Slutsker, I.; Schafer, J.; Sorokin, M.G.; Smirnov, A.; Eck, T.F.; Holben, B.; Welton, E.J. Uncertainty and Bias in AERONET Nighttime AOD Measurements. In *AGU Fall Meeting Abstracts*; American Geophysical Union: Washington, DC, USA, 2019; Volume 2019, p. A23R-3050.
36. Peng, J.; Hu, M.; Shang, D.; Wu, Z.; Du, Z.; Tan, T.; Wang, Y.; Zhang, F.; Zhang, R. Explosive Secondary Aerosol Formation during Severe Haze in the North China Plain. *Environ. Sci. Technol.* **2021**, *55*, 2189–2207. [[CrossRef](#)] [[PubMed](#)]
37. Kim, K.N.; Kim, S.H.; Park, S.S.; Lee, Y.G. Feasibility Analysis of AERONET Lunar AOD for Nighttime Particulate Matter Estimation. *Environ. Res. Commun.* **2023**, *5*, 051004. [[CrossRef](#)]
38. Ma, Z.; Hu, X.; Huang, L.; Bi, J.; Liu, Y. Estimating Ground-Level PM_{2.5} in China Using Satellite Remote Sensing. *Environ. Sci. Technol.* **2014**, *48*, 7436–7444. [[CrossRef](#)] [[PubMed](#)]
39. Rohen, G.J.; Von Hoyningen-Huene, W.; Kokhanovsky, A.; Dinter, T.; Vountas, M.; Burrows, J.P. Retrieval of Aerosol Mass Load (PM10) from MERIS/Envisat Top of Atmosphere Spectral Reflectance Measurements over Germany. *Atmos. Meas. Tech.* **2011**, *4*, 523–534. [[CrossRef](#)]
40. Koelemeijer, R.B.A.; Homan, C.D.; Matthijsen, J. Comparison of Spatial and Temporal Variations of Aerosol Optical Thickness and Particulate Matter over Europe. *Atmos. Environ.* **2006**, *40*, 5304–5315. [[CrossRef](#)]
41. Estellés, V.; Martínez-Lozano, J.A.; Pey, J.; Sicard, M.; Querol, X.; Esteve, A.R.; Utrillas, M.P.; Sorribas, M.; Gangoiiti, G.; Alastuey, A.; et al. Study of the Correlation between Columnar Aerosol Burden, Suspended Matter at Ground and Chemical Components in a Background European Environment. *J. Geophys. Res. Atmos.* **2012**, *117*, D04201. [[CrossRef](#)]
42. Seo, S.; Kim, J.; Lee, H.; Jeong, U.; Kim, W.; Holben, B.N.; Kim, S.-W.; Song, C.H.; Lim, J.H. Estimation of PM10 Concentrations over Seoul Using Multiple Empirical Models with AERONET and MODIS Data Collected during the DRAGON-Asia Campaign. *Atmos. Chem. Phys.* **2015**, *15*, 319–334. [[CrossRef](#)]
43. Zheng, C.; Zhao, C.; Zhu, Y.; Wang, Y.; Shi, X.; Wu, X.; Chen, T.; Wu, F.; Qiu, Y. Analysis of Influential Factors for the Relationship between PM_{2.5} and AOD in Beijing. *Atmos. Chem. Phys.* **2017**, *17*, 13473–13489. [[CrossRef](#)]

44. Dee, D.P.; Uppala, S.M.; Simmons, A.J.; Berrisford, P.; Poli, P.; Kobayashi, S.; Andrae, U.; Balmaseda, M.A.; Balsamo, G.; Bauer, P.; et al. The ERA-Interim Reanalysis: Configuration and Performance of the Data Assimilation System. *Q. J. R. Meteorol. Soc.* **2011**, *137*, 553–597. [[CrossRef](#)]
45. Fan, X.; Nie, G.; Deng, Y.; An, J.; Song, P.; Li, H.; Gu, Y. Influence of Earthquake on the Atmospheric Aerosols Study Using Aeronet Retrieved Aerosol Optical Depth. In Proceedings of the 2016 IEEE International Geoscience and Remote Sensing Symposium (IGARSS), Beijing, China, 10–15 July 2016; pp. 4080–4083.
46. Fan, Z.; Zhan, Q.; Yang, C.; Liu, H.; Bilal, M. Estimating PM_{2.5} Concentrations Using Spatially Local Xgboost Based on Full-Covered SARA AOD at the Urban Scale. *Remote Sens.* **2020**, *12*, 3368. [[CrossRef](#)]
47. Peng, J.; Han, H.; Yi, Y.; Huang, H.; Xie, L. Machine Learning and Deep Learning Modeling and Simulation for Predicting PM_{2.5} Concentrations. *Chemosphere* **2022**, *308*, 136353. [[CrossRef](#)]
48. Zhang, J.; Zhang, H.; Wang, R.; Zhang, M.; Huang, Y.; Hu, J.; Peng, J. Measuring the Critical Influence Factors for Predicting Carbon Dioxide Emissions of Expanding Megacities by XGBoost. *Atmosphere* **2022**, *13*, 599. [[CrossRef](#)]
49. Snoek, J.; Larochelle, H.; Adams, R.P. Practical Bayesian Optimization of Machine Learning Algorithms. In Proceedings of the Advances in Neural Information Processing Systems, Lake Tahoe, NV, USA, 3–6 December 2012; Curran Associates, Inc.: New York, NY, USA, 2012; Volume 25.
50. Ma, Y.; Zhang, W.; Zhang, L.; Gu, X.; Yu, T. Estimation of Ground-Level PM_{2.5} Concentration at Night in Beijing-Tianjin-Hebei Region with NPP/VIIRS Day/Night Band. *Remote Sens.* **2023**, *15*, 825. [[CrossRef](#)]
51. Ma, Y.; Zhang, W.; Chen, X.; Zhang, L.; Liu, Q. High Spatial Resolution Nighttime PM_{2.5} Datasets in the Beijing–Tianjin–Hebei Region from 2015 to 2021 Using VIIRS/DNB and Deep Learning Model. *Remote Sens.* **2023**, *15*, 4271. [[CrossRef](#)]
52. Wei, J.; Huang, W.; Li, Z.; Xue, W.; Peng, Y.; Sun, L.; Cribb, M. Estimating 1-Km-Resolution PM_{2.5} Concentrations across China Using the Space-Time Random Forest Approach. *Remote Sens. Environ.* **2019**, *231*, 111221. [[CrossRef](#)]
53. Ma, J.; Zhang, R.; Xu, J.; Yu, Z. MERRA-2 PM_{2.5} Mass Concentration Reconstruction in China Mainland Based on LightGBM Machine Learning. *Sci. Total Environ.* **2022**, *827*, 154363. [[CrossRef](#)] [[PubMed](#)]
54. Zhang, W.; Gu, X.; Xu, H.; Yu, T.; Zheng, F. Assessment of OMI near-UV Aerosol Optical Depth over Central and East Asia. *J. Geophys. Res. Atmos.* **2016**, *121*, 382–398. [[CrossRef](#)]
55. Zhang, W.; Xu, H.; Zheng, F. Aerosol Optical Depth Retrieval over East Asia Using Himawari-8/AHI Data. *Remote Sens.* **2018**, *10*, 137. [[CrossRef](#)]
56. Zhang, W.; Xu, H.; Zhang, L. Assessment of Himawari-8 AHI Aerosol Optical Depth Over Land. *Remote Sens.* **2019**, *11*, 1108. [[CrossRef](#)]
57. Sun, L.; Li, R.-B.; Tian, X.-P.; Wei, J. Analysis of the Temporal and Spatial Variation of Aerosols in the Beijing-Tianjin-Hebei Region with a 1 Km AOD Product. *Aerosol Air Qual. Res.* **2017**, *17*, 923–935. [[CrossRef](#)]

Disclaimer/Publisher’s Note: The statements, opinions and data contained in all publications are solely those of the individual author(s) and contributor(s) and not of MDPI and/or the editor(s). MDPI and/or the editor(s) disclaim responsibility for any injury to people or property resulting from any ideas, methods, instructions or products referred to in the content.